nature catalysis

ARTICLES

https://doi.org/10.1038/s41929-019-0293-8

Dynamic coordination of cations and catalytic selectivity on zinc–chromium oxide alloys during syngas conversion

Sicong Ma, Si-Da Huang and Zhi-Pan Liu*

Metal oxide alloys (for example $A_xB_yO_z$) exhibit dramatically different catalytic properties in response to small changes in composition (the A:B ratio). Here, we show that for the ternary zinc–chromium oxide (ZnCrO) catalysts the activity and selectivity during syngas (CO/H_2) conversion strongly depend on the Zn:Cr ratio. By using a global neural network potential, stochastic surface walking global optimization and first principles validation, we constructed a thermodynamics phase diagram for Zn–Cr–O that reveals the presence of a small stable composition island, that is, Zn:Cr:O = 6:6:16 to 3:8:16, where the oxide alloy crystallizes into a spinel phase. By changing the Zn:Cr ratio from 1:2 to 1:1, the ability to form oxygen vacancies increases appreciably and extends from the surface to the subsurface, in agreement with previous experiments. This leads to the critical presence of a four-coordinated planar Cr^{2+} cation that markedly affects the syngas conversion activity and selectivity to methanol, as further proved by microkinetics simulations.

Metal oxide alloys (MOAs) have long been utilized as the essential building block for many functional materials. In heterogeneous catalysis, MOAs not only commonly act as supporting materials but also directly catalyse a wide range of reactions. Zinc–chromium oxide (ZnCrO), for example, is well established as a catalyst for the conversion of syngas (CO/H_2) into methanol and other chemicals[1,2], and has gained much recent attention as a key ingredient in the oxide–zeolite composite catalysts for syngas-to-alkene conversion[3]. Compared to metal and metal alloys, our current understanding of MOAs falls short of expectation, not least because of their compositional variability and the associated complexity in atomic structures. One major problem associated with ZnCrO is that its thermodynamic phase diagram remains largely unknown, as do the catalytic kinetics on different surfaces with variable compositions. To establish a linkage correlation between the atomic structures of MOAs and their properties is thus a major challenge.

As one of the first-generation industry catalysts for the syngas-to-methanol reaction[4], ZnCrO has been extensively studied since 1930s. It is now generally believed that $ZnCr_2O_4$ with a spinel crystal form is the most stable phase as it forms after calcination at high temperature[5]. However, catalysts with Zn:Cr ratios above 1:2 (Zn rich) were also synthesized. The atomic structure of these catalysts with Zn:Cr ratios between 1:1 and 1:2 remains, however, uncertain as no clear evidence of ZnO formation was found, although the X-ray diffraction patterns exhibit peak broadening and small peak shifts compared to the $ZnCr_2O_4$ spinel phase[6–8]. Further increasing the Zn:Cr ratios (>1:1), ZnO aggregation in the catalysts was detected by X-ray diffraction, but the quantitative analysis shows that the amount of ZnO is far less than the theoretical value if the catalyst is assumed to be composed of $ZnCr_2O_4$ and ZnO (refs. [6,7]). The experimental data imply that some unknown MOA phases may be present within the ZnCrO ternary potential energy surface (PES).

For the catalytic kinetics, many research groups showed that the Zn:Cr ratios can significantly influence the syngas-to-methanol catalytic activity and selectivity[2,6,9,10]. Interestingly, the best activity and selectivity is generally achieved in the window Zn:Cr = 1:1 to 2:1, for example, a methanol yield of ~90 $g\,kg_{cat}^{-1}\,h^{-1}$ and a selectivity of 80% for Zn:Cr = 1:1 (ref. [6]). The pure $ZnCr_2O_4$ spinel catalysts, by contrast, yield rather poor activity and selectivity, <5 $g\,kg_{cat}^{-1}\,h^{-1}$ and 14% selectivity to methanol (~45% to alkane)[6]. Given that the increase of the Zn:Cr ratios shifts the H_2 reduction peak to the low-temperature region[6,11], it was suggested that the activity and selectivity dependence on the Zn:Cr ratios might be due to the ability to form an oxygen vacancy (O_v) that constitutes the active site. However, owing to the structural uncertainty for ZnCrO phases above 1:2, no quantitative data on the structure stability and O_v formation energetics are available to date. The lack of knowledge on the active site hinders the further optimization of the syngas conversion performance on ZnCrO catalysts and the related oxide–zeolite catalytic systems.

To link the atomic structure of ZnCrO with its catalytic activity, it is critical to explore the vast structural space of the ternary system and identify the structural motif relevant to the reaction conditions. Here, by combining a global machine learning potential and an efficient global PES sampling, we were able to follow the ZnCrO structural evolution with changes in the Zn:Cr:O ratio and establish the Zn–Cr-O ternary phase diagram. An active $Zn_3Cr_3O_8$ metastable crystal phase was identified and the exposure of four-coordinated planar Cr^{2+} cations under the reaction conditions was found to be responsible for catalysing the syngas to methanol.

Results

Zn–Cr–O ternary phase diagram. Our investigation started from the thermodynamic phase space and scanned for bulk ZnCrO structures with the Zn:Cr:O ratios running from CrO_x to ZnO, as mapped in the Zn–Cr–O ternary phase diagram in Fig. 1a with pure CrO, CrO_3 and ZnO as the vertexes. For each ratio, more than 10,000 minima were visited on the PES by stochastic surface walking (SSW)[12–16] global optimization together with the high-dimensional

Collaborative Innovation Centre of Chemistry for Energy Material, Shanghai Key Laboratory of Molecular Catalysis and Innovative Materials, Key Laboratory of Computational Physical Science, Department of Chemistry, Fudan University, Shanghai, China. *e-mail: zpliu@fudan.edu.cn

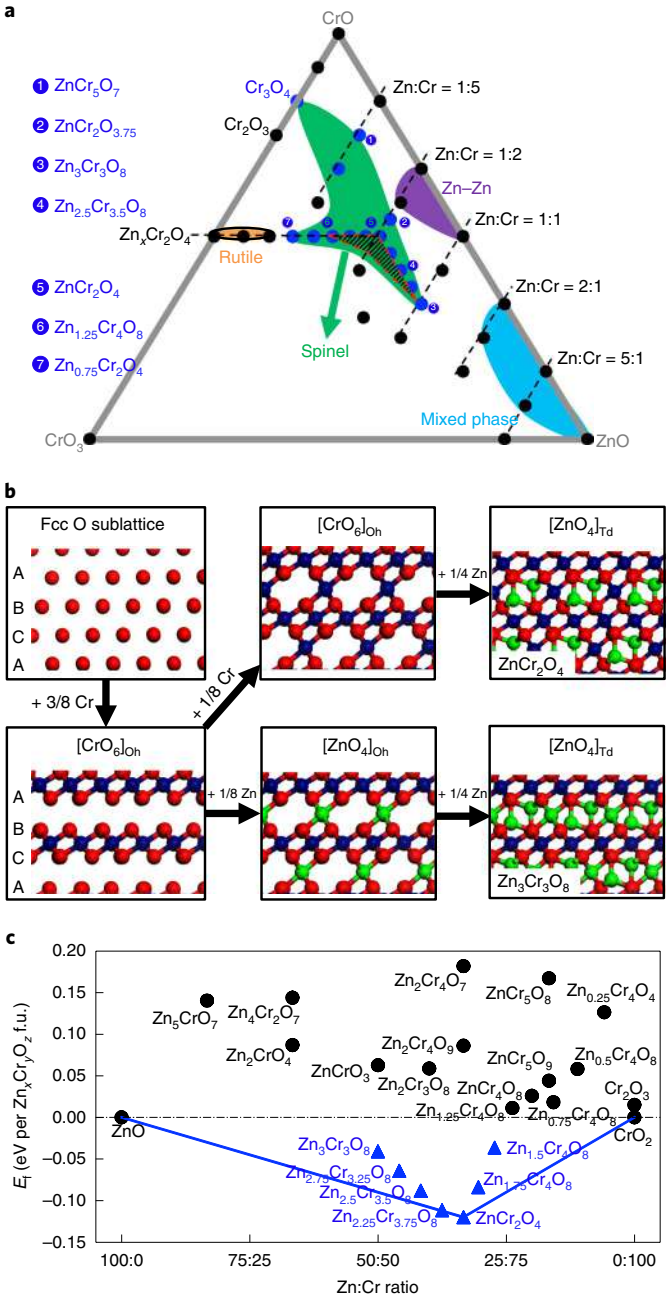

Fig. 1 | Thermodynamics and structures of bulk ZnCrO at different compositions. a, Ternary Zn–Cr–O phase diagram. The green region maps out that the compositions with the spinel-type skeleton structure as the global minimum; the blue circles labelled by numbers indicate the composition. Only the spinel ZnCrO phases in the red dashed triangle are thermodynamically allowed (see **c**). **b**, Illustration of the structure motifs of the spinel $ZnCr_2O_4$ ($Fd\bar{3}m$, no. 227) and $Zn_3Cr_3O_8$ ($R\bar{3}m$, no. 166) bulk. Zn, green; Cr, purple; O, red. **c**, Convex hulls for all the ZnCrO structures are indicated by the blue line. The blue triangles and black circles represent the negative and positive formation energy compared to the ZnO and CrO_2 phases, respectively. f.u., formula unit.

neural network (NN) potential[17–19] (SSW–NN) with an atom number per unit cell that ranges from 12 to 56, in total >500,000 minima for all ratios. The PESs of partial ZnCrO compositions are given in Supplementary Fig. 1. This exhaustive search covers the likely chemical compositions with the valence states of Cr from +2 to +6 and includes the mixed +3/+4 and +2/+3 states if Zn^{2+} and O^{2-} are assumed. We summarize the global minima structures in Fig. 1a.

First, the spinel-type crystalline structures appear as a major structure motif for the ZnCrO in the range Zn:Cr = 0:1 to Zn:Cr = 1:1, as indicated by green in Fig. 1a. The $ZnCr_2O_4$ crystal known from experiments falls in this region. These crystals generally have a face-centred cubic (fcc) sublattice formed by O^{2-} anions, but with different Zn and Cr occupations in the interstitial tetrahedral (Td) and octahedral (Oh) sites. As illustrated in Fig. 1b, the fcc O sublattice with [ABCABC] stacking provides eight Td and four Oh sites per fcc unit cell. For the typical $ZnCr_2O_4$ spinel ($Fd\bar{3}m$, no. 227), the Oh sites in the [BC] interlayer are occupied by 3/8 Cr atoms relative to the total O atoms, and the Oh and Td sites in the [AB]([CA]) interlayer is occupied by 1/8 Cr and 1/4 Zn atoms, respectively. In total, Zn and Cr atoms occupy one-eighth of Td and half of the Oh sites, respectively. The structural formula can be written as $[Zn^{2+}]_{Td}[Cr_2^{3+}]_{Oh}O_4$. The other spinel crystalline phases, which include the newly identified $Zn_{3-x}Cr_{3+x}O_8$ ($0 \le x < 1$) and $Zn_xCr_4O_8$ ($0.75 \le x < 2$) and the known Cr_3O_4 phases, differ from the $ZnCr_2O_4$ spinel mainly in the relative concentration of Zn and Cr in the [AB]([CA]) interlayer. For example, in $Zn_3Cr_3O_8$ ($R\bar{3}m$, no. 166), only Zn atoms are present in the [AB]([CA]) interlayer, that is, all the O_h Cr atoms in the [AB]([CA]) interlayer are replaced by Zn atoms from $ZnCr_2O_4$, with the structural formula $[Zn^{2+}_2]_{Td}[Zn^{2+}Cr_2^{3+}Cr^{4+}]_{Oh}O_8$ (Fig. 1b). The lattice parameters are given in Supplementary Table 1. However, in Cr_3O_4 ($I4_1/amd$, no. 141), all the Td Zn atoms in the [AB]([CA]) interlayer are replaced by Cr atoms from $ZnCr_2O_4$ with the structural formula of $[Cr^{2+}]_{Td}[Cr_2^{3+}]_{Oh}O_4$.

Second, with the depletion of O atoms, the ZnCrO compositions move from the green region to the purple one with the ratio Zn:Cr = 1:2 to 1:1 and start to lose the O fcc sublattice to generally only have low symmetry forms. In particular, Zn–Zn metallic bonds appear in these compositions (Supplementary Fig. 2), which indicates the preference to keep Cr–O bonds instead of Zn–O bonds when O depletes.

Third, with the depletion of Zn atoms, the ZnCrO compositions move from the green region towards CrO_2 with the ratio Zn:Cr < 1:8 (the orange region) and adopt the rutile type CrO_2 lattice with Zn doping in the rutile interstitial sites (Supplementary Fig. 2).

Fourth, with the depletion of Cr atoms, the ZnCrO compositions move from the green region towards the vertex ZnO with the ratio Zn:Cr > 2:1 (the blue region) and prefer a mixed ZnO (wurtzite/zinc blende) and layered CrO_2 structure (MoS_2 type) packed together via different linkages (for example, $[CrO_5]$ and Zn–O–Cr in Supplementary Fig. 2). The presence of these heterostructures implies a good lattice matching between the ZnO crystal and layered CrO_2.

Taking the formation energy (E_f) of all these ZnCrO global minima, we computed the thermodynamic convex hull of ZnCrO compounds at different Zn:Cr ratios as plotted in Fig. 1c. All the energetics are referred to the most stable pure phases, the wurtzite ($P6_3mc$, no. 186) ZnO and the rutile-type ($P4_2/mnm$, no. 136) CrO_2 phases.

Interestingly, the convex hull shows that only a small range of ZnCrO compositions with a spinel-type skeleton, that is, $Zn_{3-x}Cr_{3+x}O_8$ ($0 \le x \le 1$) and $Zn_xCr_4O_8$ ($1.5 \le x < 2$), have a negative formation energy, and the $ZnCr_2O_4$ spinel phase is, not surprisingly, the most stable phase with the largest exothermic formation. Moreover, as the Zn:Cr ratio deviates from 1:2, these spinel structures become less stable in reference to $ZnCr_2O_4$, ZnO and CrO_2. Our results confirm that Zn:Cr ratios above 1:1 and below 3:8 are highly unstable—no stable crystalline phases (positive formation energy) are present according to the thermodynamics, which suggests a strong tendency of phase segregation towards $ZnCr_2O_4$, ZnO and CrO_2. For the metastable spinel phases with Zn:Cr ratios between 1:1 and 3:8 near to $ZnCr_2O_4$, their fates may

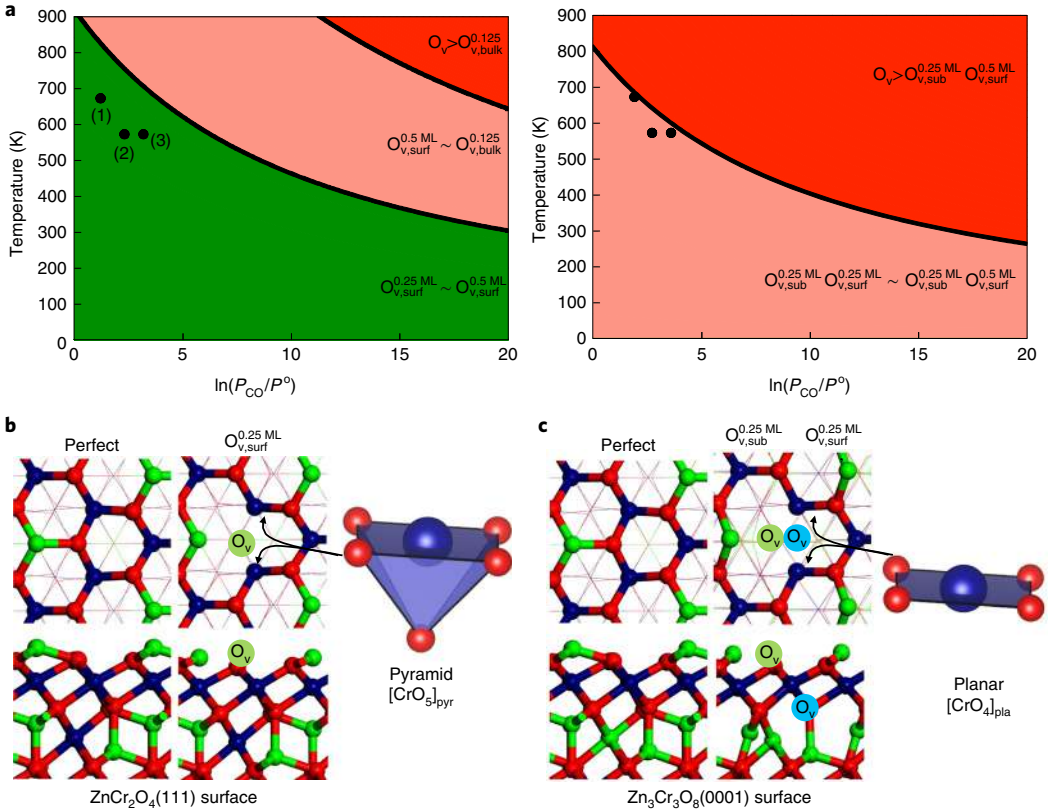

Fig. 2 | Surface structures and phase diagram for $ZnCr_2O_4$ and $Zn_3Cr_3O_8$ crystals under reaction conditions. a, Thermodynamic phase diagram for $ZnCr_2O_4$ (left) and $Zn_3Cr_3O_8$ (right) in contact with CO at different temperatures and pressures (P). The phase diagram is computed based on Gibbs free energy data for the reaction ($Zn_xCr_yO_z + nCO \rightarrow Zn_xCr_yO_{z-n} + nCO_2$) from DFT calculations assuming a CO_2 pressure of 0.1 kPa. Green and red represent the absence and presence, respectively, of subsurface/bulk O_v ($O_{v,sub}$/$O_{v,bulk}$). Typical experimental conditions for syngas conversion from the literature ((1) Jiao et al.[3], (2) Song et al.[6] and (3) Tian et al.[24]) are also shown. P^o represents the standard pressure (101.325 kPa). **b**,**c**, The perfect O_v containing $ZnCr_2O_4$ $O^{0.25\ ML}_{v,surf}$(111) and $Zn_3Cr_3O_8$ $O^{0.25\ ML}_{v,surf}O^{0.25\ ML}_{v,sub}$(0001) surface structures. The $[CrO_5]_{pyr}$ and $[CrO_4]_{pla}$ configurations near to an O_v are highlighted. The surface/subsurface O_v concentration of 0.25 ML with respect to all the O atoms in the same layer is denoted as $O^{0.25\ ML}_{v,surf}$/$O^{0.25\ ML}_{v,sub}$.

strongly depend on the synthetic conditions (for example, temperature)—once these spinel crystalline structures are synthesized, they should be kinetically stable as the solid disproportionation reaction ($Zn_xCr_yO_z \rightarrow ZnCr_2O_4 + ZnO/CrO_2$) is generally slow. We note that for the sample with Zn:Cr = 1:1, the ZnO aggregation starts to appear only after a high-temperature (753 K) calcination experiment[7,8].

Surface properties of $Zn_3Cr_3O_8$ and $ZnCr_2O_4$. As our thermodynamics diagram on the bulk compositions suggests that only spinel structures with Zn:Cr from 3:8 to 1:1 are likely to be present under the catalytic reaction conditions, we focused on two key compositions in this range, Zn:Cr = 1:2 and 1:1 with a spinel crystalline form. The newly identified spinel $Zn_3Cr_3O_8$ that gives the highest concentration of the unusual $[ZnO_6]_{Oh}$ in bulk is a good representative for the Zn:Cr > 1:2 catalysts, which are experimentally known for a high activity towards methanol synthesis. The thermodynamically most stable $ZnCr_2O_4$, however, has the highest concentration of $[CrO_6]_{Oh}$ in bulk and Td only in $[ZnO_4]$, and can only catalyse syngas to methane at a high temperature[20]. A comparison between these two materials would thus provide deep insights into the origin for the dependence of the syngas conversion activity on the Zn:Cr ratios.

To identify the active sites of the $Zn_3Cr_3O_8$ and $ZnCr_2O_4$ catalysts, we considered a range of possible low Miller index surfaces, which included $ZnCr_2O_4$(100), (110) and (111), and $Zn_3Cr_3O_8$(0001), ($11\bar{2}1$), ($11\bar{2}0$) and ($10\bar{1}1$). By computing their surface energies (γ (Supplementary Table 2 and Supplementary Fig. 3)), we found that the most stable surfaces are close-packed (0001) ($\gamma = 0.66\ J\ m^{-2}$) and (111) ($\gamma = 0.75\ J\ m^{-2}$) for $Zn_3Cr_3O_8$ and $ZnCr_2O_4$, respectively. These two surfaces basically show the same first-layer structure, which features honeycomb-interlinked Zn–O–Cr six-membered rings with exposed three-coordinated Zn_{3c}, three-coordinated O_{3c} and six-coordinated Cr_{6c} atoms (Fig. 2b,c). The major differences between these two surfaces are the Zn coordination and position at the subsurface, where the Zn cations occupy both Td and Oh sites in $Zn_3Cr_3O_8$, but only occupy Td sites in $ZnCr_2O_4$.

Under the syngas reaction conditions, these ZnCrO surfaces should undergo reduction by reacting with CO/H_2 to form CO_2/H_2O. To determine the equilibrium O_v concentration in ZnCrO bulk and surfaces, ab initio thermodynamics analyses were performed with equation (1) to compute the Gibbs free energy change (ΔG) as the function of temperature and CO/H_2 partial pressure:

$$Zn_xCr_yO_z + nCO/H_2 \rightarrow Zn_xCr_yO_{z-n} + nCO_2/H_2O \quad (1)$$

As we found that CO has a stronger reductive ability than H_2, the phase diagram under CO conditions is presented in Fig. 2a and elaborated below (the phase diagram under H_2 conditions is shown in Supplementary Fig. 4). In Fig. 2a, green and red represent the absence and presence, respectively, of bulk/subsurface O_v. As shown, an increase of temperature and CO pressure means the gradual increase of the O_v concentration in the system, that is, from the first-layer surface O_v ($O_{v,surf}$) to the subsurface O_v ($O_{v,sub}$) and to

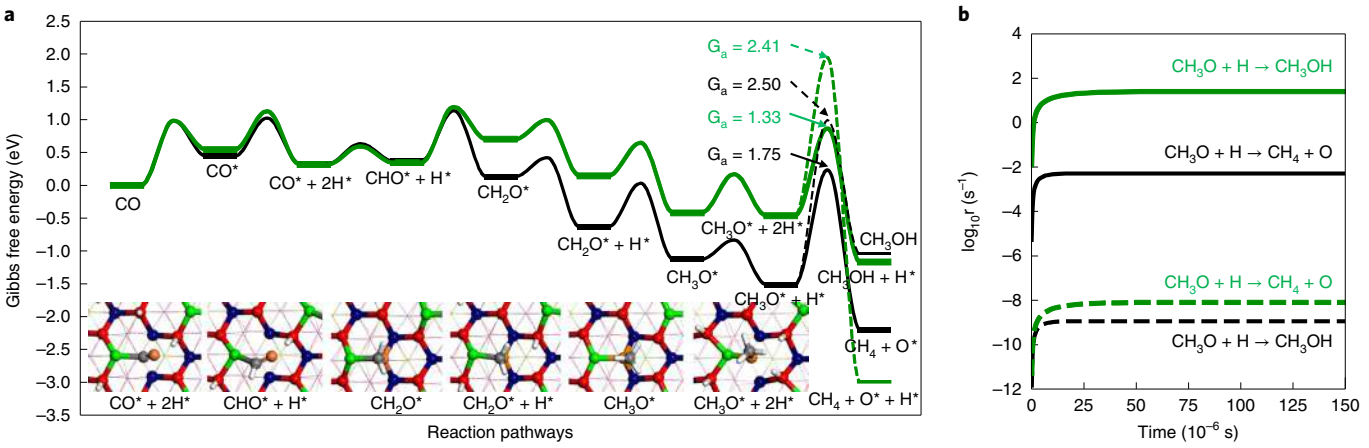

Fig. 3 | Syngas conversion mechanisms and kinetics. a,**b**, Gibbs free energy reaction profiles (**a**) and microkinetics simulation (**b**) for syngas conversion rates on two ZnCrO catalysts at 573 K and 2.5 MPa syngas (H_2:CO = 1.5). In both figures, the black and green lines represent the $ZnCr_2O_4$ $O_{v,surf}^{0.25\ ML}$(111) and $Zn_3Cr_3O_8$ $O_{v,surf}^{0.25\ ML}O_{v,sub}^{0.25\ ML}$(0001) surfaces, respectively. The asterisk indicates the adsorption state. The reaction snapshots are shown in the inset of **a:** Zn, green; Cr, purple; O, red; O in CO, orange; C, grey; H, white.

bulk O_v ($O_{v,bulk}$). All the O_v formation energies at different sites are summarized in Supplementary Table 3.

In general, with an increase in temperature and CO pressure, the concentration of O_v increases for both $Zn_3Cr_3O_8$ and $ZnCr_2O_4$. In comparing $Zn_3Cr_3O_8$ with $ZnCr_2O_4$, we found that $Zn_3Cr_3O_8$ can be reduced more facilely—under the normal catalytic reaction conditions (~300–700 K, CO pressure ~0.1–20 MPa), $O_{v,sub}$ or $O_{v,bulk}$ already form in $Zn_3Cr_3O_8$, but are absent in $ZnCr_2O_4$. Under 573 K and 1 MPa CO pressure conditions (typical experimental conditions for syngas conversion), the $Zn_3Cr_3O_8$(0001) surface not only has a surface O_v concentration between 0.25 monolayers (ML, with respect to all the O atoms at the same layer, denoted as $O_{v,surf}^{0.25\ ML}$) and 0.5 ML, but also generates a 0.25 ML subsurface O_v ($O_{v,sub}^{0.25\ ML}$). By contrast, $ZnCr_2O_4$ only has surface O_v with a concentration between 0.25 and 0.5 ML.

Figure 2b,c shows the optimized geometry structures for the $ZnCr_2O_4$ $O_{v,surf}^{0.25\ ML}$(111) and $Zn_3Cr_3O_8$ $O_{v,surf}^{0.25\ ML}O_{v,sub}^{0.25\ ML}$(0001) surfaces that are thermodynamically allowed under the reaction conditions. After losing the 0.25 ML surface O, the $ZnCr_2O_4$(111) surface exposes one two-coordinated Zn atom and two five-coordinated Cr_{5c} atoms with the pyramid configuration ($[CrO_5]_{pyr}$) near to an O_v (Fig. 2b). The formation of an O_v means that the $[CrO_5]_{pyr}$ has an increased magnetic moment of 3.16 μB relative to 2.98 μB of the perfect surface and close to that of the bulk Cr_2O_3 (3.07 μB), which indicates that the $[CrO_5]_{pyr}$ is still Cr^{3+} in the oxidation state.

By contrast, after losing the 0.25 ML surface and the 0.25 ML subsurface O atoms, the $Zn_3Cr_3O_8$(0001) surface generates one Zn_{2c} atom and two Cr_{4c} atoms with the planar configuration ($[CrO_4]_{pla}$) near to an O_v (Fig. 2c). The $[CrO_4]_{pla}$ has a magnetic moment of 3.54 μB, which is close to that of CrO (3.81 μB in bulk and 3.61 μB on the CrO(100) surface), much higher than that in Cr_2O_3 and CrO_2 (2.47 μB). This suggests that the $[CrO_4]_{pla}$ is more like a Cr^{2+} in the oxidation state.

As only the thermodynamics are evaluated in Fig. 2a, we also checked whether an O_v can migrate at elevated temperatures (for example 573 K) in $Zn_3Cr_3O_8$. To this end, we investigated the O_v migration from the surface to the subsurface on the $Zn_3Cr_3O_8$(0001) surface (that is, lattice O diffusion from the subsurface to the surface). For the 0.5 ML surface O_v, the lattice O diffusion is exothermic by 0.76 eV and the diffusion barrier is 1.48 eV (triangular pyramid $[CrO_4]$ to $[CrO_4]_{pla}$), which finally yields the 0.25 ML surface O_v and the 0.25 ML subsurface O_v. The reaction barrier of O_v diffusion is similar to that in the syngas conversion, as presented below. This concludes that the presence of bulk/subsurface O_v is not only thermodynamically possible, but also kinetically feasible under the reaction conditions.

Reaction mechanisms for syngas conversion. With the knowledge on the surface structures under the reaction conditions, we can now evaluate the syngas conversion activity of two catalysts, as represented by the $O_{v,surf}^{0.25\ ML}$(111) and $O_{v,surf}^{0.25\ ML}O_{v,sub}^{0.25\ ML}$(0001) surfaces. The Gibbs free energy reaction profiles are shown in Fig. 3a. The temperature and CO/H_2 pressure are assumed to be at typical reaction conditions, that is, 573 K and 2.5 MPa (H_2:CO = 1.5). On both surfaces, our calculations support the stepwise hydrogenation mechanism in syngas conversion, CO → CHO → CH_2O → CH_3O → CH_3OH/CH_4.

Taking the reaction on $Zn_3Cr_3O_8$ as the example, the reaction starts by CO adsorption with an exothermic energy of 0.44 eV (Supplementary Table 4). At a high temperature (573 K), the adsorption becomes endothermic with a free energy cost of 0.54 eV due to the entropy losses. Next, H_2 can dissociate nearby the surface O_v involving two exposed O sites (Supplementary Fig. 5). The free energy barrier is 0.58 eV and the reaction is exothermic by 0.22 eV at 573 K. In the presence of a nearby H, the CO can react sequentially with the H atom to form CHO and CH_2O. The reaction barriers for these two hydrogenation reactions are 0.27 and 0.85 eV with reaction energies of 0.03 and 0.36 eV, respectively. The formaldehyde CH_2O may desorb given that its adsorption energy is only 0.57 eV. Alternatively, it may further react with a nearby H atom to produce CH_3O with an energy barrier of 0.50 eV, a reaction that is exothermic by 0.56 eV. The formed CH_3O stays at the O_v site, bonding with a neighbouring surface Zn_{2c} and two Cr_{4c} atoms. The formed Zn–O and Cr–O bond distances are 1.99 and 2.05 Å, respectively. The surface then can accommodate two adsorbed hydrogen atoms with an exothermic energy of 0.90 eV ($\Delta G = -0.05$ eV). The CH_3O group is hydrogenated into CH_3OH or CH_4 depending on whether the C or O in CH_3O reacts with the incoming H. On the $Zn_3Cr_3O_8$ surface, the reaction channel to CH_3OH is kinetically much more facile with a reaction barrier of 1.33 eV, whereas that to CH_4 formation has a 2.41 eV reaction barrier. Our calculated reaction barrier for methanol on the $Zn_3Cr_3O_8$ surface agrees well with the apparent experimental activation energy of ~1.20 eV (113 ± 5 kJ mol^{-1}) reported by Errani et al.[9].

Compared to the reaction on the $Zn_3Cr_3O_8$ surface, the syngas conversion on $ZnCr_2O_4$ prefers the formation of CH_4 instead of CH_3OH. As shown in the reaction profiles in Fig. 3a, the major

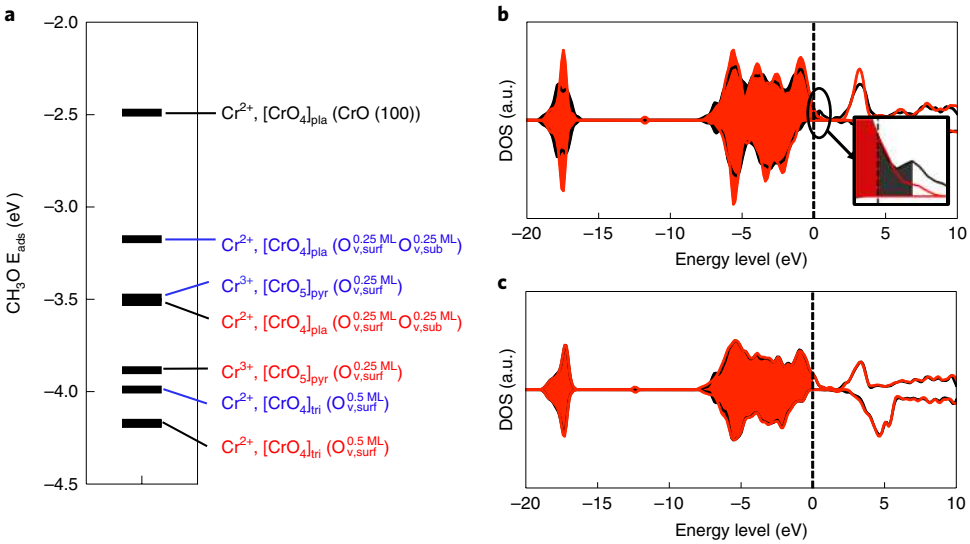

Fig. 4 | Energetics and electronic structure analyses of CH_3O adsorption. a, Comparison of CH_3O adsorption energies (E_{ads}) on $ZnCr_2O_4$(111) (red) and $Zn_3Cr_3O_8$(0001) (blue) surfaces at different O_v concentrations. The adsorption energy is with respect to the gas phase CH_3O radical. **b**,**c**, DOS before (black) and after (red) CH_3O adsorption on the $ZnCr_2O_4$ $O^{0.25\ ML}_{v,surf}$(111) (**b**) and $Zn_3Cr_3O_8$ $O^{0.25\ ML}_{v,surf}O^{0.25\ ML}_{v,sub}$(0001) (**c**) surfaces. The filled regions represent the occupied states. The DOS curves are aligned with the bulk valence band and the Fermi energy level after CH_3O adsorption is set as zero. The inset in **b** highlights the states near to the Fermi level before and after CH_3O adsorption on $ZnCr_2O_4$ and shows the obvious difference in electron occupation induced by CH_3O adsorption. a.u., arbitrary units.

differences between the two catalysts are the adsorption energy of CH_2O and CH_3O. The $ZnCr_2O_4$ surface, although it is less reductive with only a 0.25 ML surface O_v, can adsorb oxygen-containing species much more strongly, CH_3O in particular. The CH_3O adsorption on $ZnCr_2O_4$ releases 3.88 eV of energy with respect to the CH_3O radical in the gas phase, and is 0.71 eV larger than that on the $Zn_3Cr_3O_8$ surface. The surface then can accommodate only one hydrogen atom with an exothermic energy of 0.83 eV ($\Delta G = -0.38$ eV). Owing to the large adsorption energy of CH_3O on $ZnCr_2O_4$, the hydrogenation for CH_3O selects the methane formation channel with a reaction barrier of 1.75 eV (the reaction to give CH_3OH has much higher barriers of 2.50 eV). Once CH_4 is formed, the surface can recover its surface O_v with the aid of H_2/CO. This is thermodynamically favoured, as shown in Fig. 2a. Kinetically, H_2 molecule can react with the surface O to produce H_2O and generate O_v, which is calculated to have an overall barrier of 1.47 eV, much lower than the 1.75 eV for methane production on $ZnCr_2O_4$ (Supplementary Fig. 6).

From the overall reaction profiles, we can now determine the reaction rate of syngas conversion on the $ZnCr_2O_4$ $O^{0.25\ ML}_{v,surf}$(111) and $Zn_3Cr_3O_8$ $O^{0.25\ ML}_{v,surf}O^{0.25\ ML}_{v,sub}$(0001) surfaces based on microkinetics simulation. All the kinetics data are obtained from the above results and listed in Supplementary Table 5. Our microkinetics numerical simulation results are shown in Fig. 3b. We found that the surface O_v sites and exposed O atoms act as the reaction site and reservoir for H_2 dissociation. Both surfaces are quickly covered by CH_3O groups and H atoms (99.9% occupancy), within 10^{-6} s, when the CO hydrogenation reaction reaches a steady state, as shown in Fig. 3b. This proves that the consumption of CH_3O is the rate-determining step on both surfaces.

The key difference between the two surfaces is the selectivity. On the $Zn_3Cr_3O_8$ surface, CH_3O hydrogenation to give CH_3OH is much faster than that to CH_4, but it is just the opposite for the $ZnCr_2O_4$ surface. At 573 K, a typical experimental temperature, the turnover frequency of CH_3OH production on $Zn_3Cr_3O_8$ surface is ~250 s^{-1} which is four orders of magnitude larger than that of CH_4 production (5×10^{-3} s^{-1}) on the $ZnCr_2O_4$ surface. This methanol production activity is equivalent to ~670 $g\,kg_{cat}^{-1}\,h^{-1}$ by assuming the active-site concentration is ~1–2% on the exposed $Zn_3Cr_3O_8$ surfaces (Supplementary Information). The value compares well with the experimental data of ~80–600 $g\,kg_{cat}^{-1}\,h^{-1}$ (refs. [6,9]). However, our theoretical activity on $ZnCr_2O_4$ towards methane is only ~0.08 $g\,kg_{cat}^{-1}\,h^{-1}$ under a similar approximation for the active site concentration. Experimentally, the catalysts with the Zn:Cr = 1:2 have a very low catalytic activity at 573 K, and even at 673 K the reactions still have a low CO conversion (~0.6%) with a selectivity mainly for the hydrocarbon ~82% (91% CH_4)[6,20]. From our results, we can therefore conclude that the product selectivity to methanol or methane can be attributed largely to the different adsorption strengths of the CH_3O group. The weak CH_3O adsorption on a $Zn_3Cr_3O_8$ surface leads to the generation of CH_3OH, whereas the strong CH_3O adsorption on a $ZnCr_2O_4$ surface produces CH_4.

Origin of the CH_3O adsorption properties. Our results from the microkinetics simulation shows that the catalytic activity and selectivity differences between two different spinel phases can be largely attributed to the sensitivity of the CH_3O adsorption strength on two different surfaces. The strong adsorption of CH_3O on a $ZnCr_2O_4$ surface apparently hinders the formation of CH_3OH and also leads to a high barrier of CH_4 formation, whereas the moderate adsorption of CH_3O on a $Zn_3Cr_3O_8$ surface promotes the CH_3OH channel. It is therefore essential to analyse in depth the key factor that controls the CH_3O binding on the oxide surface.

To this end, we first investigated the adsorption energies of CH_3O on $ZnCr_2O_4$(111) and on $Zn_3Cr_3O_8$(0001) surfaces with varied O_v concentrations. The results are illustrated in Fig. 4a. We found that the planar $[CrO_4]_{pla}$ (Cr^{2+}) has the lowest energy for CH_3O adsorption, and is exposed on the $ZnCr_2O_4$(111) and $Zn_3Cr_3O_8$(0001) surfaces at an O_v concentration of $O^{0.25\ ML}_{v,surf}O^{0.25\ ML}_{v,sub}$. To confirm this, the CrO(001) surface with the exposure of $[CrO_4]_{pla}$ was constructed to examine the CH_3O adsorption, and, indeed, also shows a weak CH_3O adsorption (Supplementary Fig. 7). However, the four-coordinated Cr^{2+} with a triangular pyramid geometry ($[CrO_4]_{tri}$),

that is, $O_{v,surf}^{0.5\ ML}$, tends to bond CH_3O very strongly on both surfaces. The common $[CrO_5]_{pyr}$ (Cr^{3+}), that is $O_{v,surf}^{0.25\ ML}$, has a CH_3O adsorption energy between the two types of Cr^{2+} cation. These results suggest the Cr coordination geometry as being adjusted by different O_v concentration controls, critically the CH_3O adsorption energy.

Electronic structure analyses were then performed to understand the interaction between the surfaces and CH_3O group. The total densities of states (DOS) for the two surfaces are shown in Fig. 4b,c. For the $ZnCr_2O_4$ $O_{v,surf}^{0.25\ ML}$(111) surface, the formation of O_v leads to the partial reduction of Cr^{3+} cations near to O_v with an increase in the magnetic moments from 2.98 to 3.16 μB. Owing to the $[CrO_5]_{pyr}$ geometry, which prefers Cr^{3+}, these excess electrons have to locate above the bulk oxide valance band maximum (black circle in Fig. 4b). After CH_3O adsorption, these high-energy electrons flow towards the CH_3O group and lead to a strong CH_3O adsorption. However, for the $Zn_3Cr_3O_8$ $O_{v,surf}^{0.25\ ML}O_{v,sub}^{0.25\ ML}$(0001) surface, the excess electrons reduce the Cr^{3+} cation near to O_v to Cr^{2+} with a substantial increase in the magnetic moments from 2.98 to 3.54 μB. The planar geometry of $[CrO_4]$, the feature of Cr^{2+}, stabilizes these extra electrons. The absence of high-energy electrons, in turn, means the DOS before and after CH_3O adsorption are similar (Fig. 4c). This explains the much weaker CH_3O adsorption on a $Zn_3Cr_3O_8$ surface.

ZnCrO active sites with different Zn:Cr ratios. The relevant question in ZnCrO catalysts is the catalytic role of ZnO: whether it takes part in the syngas conversion or not. Although no ZnO aggregation was observed in catalysts with Zn:Cr ratios between 1:2 and 1:1, they were, indeed, detected for Zn:Cr ratios >1:1 (refs. [6–8]). From our phase stability diagram (Fig. 1c), the spinel form crystal is present only with Zn:Cr ratios below 1:1 and thus the ZnO phase forms at Zn:Cr > 1:1. For ZnCrO catalysts, the Zn:Cr = 1:2 to 1:1 spinel crystals, although they may degrade to $ZnCr_2O_4$ and ZnO, are kinetically stable because of the difficulty of Zn migration in bulk. In fact, this is also observed in experiments: even when the Zn:Cr ratios are >1:1, the amount of ZnO detected is far less than that in the theoretical decomposition to ZnO (some becomes $ZnCr_2O_4$)[7]. Recent experiments further demonstrate that the surface Zn:Cr ratio for different ZnCrO catalysts with an excess of Zn (Zn:Cr from 55:45 to 70:30) in the catalyst preparation converge to a ration of ~1:1 after the syngas conversion reaction according to X-ray photoelectron spectrum measurements[6]. As the reaction kinetics determined from the $Zn_3Cr_3O_8$ surface agree with the experimental data, we expect that the role of ZnO in ZnCrO-catalysed syngas conversion is not significant.

Even though the ZnO phase can be ruled out as the active site, we emphasize that Zn cations in ZnCrO catalysts play important roles. (1) The surface Zn atoms act as the best CO adsorption site, which allows the subsequent CO hydrogenation pathway. Throughout the reaction, the Zn atom is also the active site on which to coordinate the C-containing intermediates, that is, CHO, CH_2O and CH_3O (Fig. 3a). (2) The presence of $[ZnO_6]$ in the subsurface allows the formation of $[CrO_4]_{pla}$, the catalytic centre for methanol formation. As the overcoordinated $[ZnO_6]$ in $Zn_3Cr_3O_8$ tends to return to $[ZnO_4]$, the presence of the subsurface $[ZnO_6]_{O_h}$ in $Zn_3Cr_3O_8$ facilitates the creation of surface and subsurface O_v, which leads to the formation of $[CrO_4]_{pla}$. We also examined ZnCrO structures with a Zn:Cr ratio between 1:1 and 1:2, which confirmed that the presence of subsurface $[ZnO_6]$ has a strong influence on the O_v formation ability (Supplementary Fig. 8 and Supplementary Table 6). We note that $[ZnO_6]_{O_h}$ has, indeed, been detected in catalysts with Zn:Cr ratios large than 1:2 (refs. [7–9,21–24]). Also, temperature-programmed reduction of hydrogen experiments confirmed that the increase of the Zn:Cr ratios from 1:2 to 1:1 shifts the reduction peak to lower temperatures (from 663 to 583 K), consistent with the O_v phase diagram in Fig. 2a[6].

Conclusion

This work demonstrates the power of a versatile theoretical tool, machine learning potential in combination with global PES sampling, to clarify the mechanism of catalytic syngas conversion over ternary ZnCrO catalysts at different Zn:Cr ratios. By computing the bulk phase diagram, the O_v phase diagram and the reaction kinetics, we identified a planar $[CrO_4]$ site formed dynamically under syngas conversion conditions as the active centre for methanol production. Such planar $[CrO_4]$ is only available above Zn:Cr > 1:2 after the appearance of $[ZnO_6]$, the ZnCrO catalysis is highly sensitive to the Zn:Cr ratios.

The current study also provides a deeper understanding of MOA catalysts for hydrogenation reactions. In fact, a number of Zn-based MOA catalysts, such as CuZnO, ZnFeO and ZnZrO, have been found experimentally to exhibit good activity for syngas conversion or CO_2 hydrogenation reactions[20,25,26]. However, the atomic structures for these MOA catalysts remained largely unknown, but the current results on ZnCrO shed an important light on this class of catalysts. Our results demonstrate that MOAs with a versatile cation ratio enrich greatly the stable crystal structure of the catalyst. Moreover, MOA catalysts can achieve a multiple metal coordination environment and thus create diverse catalytic active sites. The catalytic properties, which include the reductive ability, the adsorption properties of molecules and reaction barriers, can thus be regulated facilely via the change of metal cation ratios, which can finally control the catalytic activity and selectivity.

Methods

SSW–NN simulation. Our approach to resolving complex oxide structures is based on the recently developed SSW–NN method as implemented in LASP code[27], where the SSW–NN achieves a fast global PES exploration. The machine learning NN potential is generated by iterative self-learning of the plane-wave density functional theory (DFT) global PES data set generated from SSW exploration. The SSW–NN simulation to explore PES can be divided into three steps: global data-set generation based on DFT calculations using selected structures from the SSW simulation, NN potential fitting and SSW global optimization using the NN potential. These steps are iteratively performed until the NN potential is transferable and robust enough to describe the global PES. The procedure is briefly summarized below.

At first, the global data set was built iteratively during the self-learning of the NN potential. The initial data of the global data set came from the DFT-based SSW simulation and all the other data were taken from the NN-based SSW PES exploration. To cover all the likely compositions of ZnCrO, SSW simulations were carried out for different structures (which included bulk, layer and cluster), compositions and atom number per unit cell (~10–84). Overall, these SSW simulations generated more than 10^7 structures on the PES. The final global data set computed from the high-accuracy DFT calculation contained 38,285 structures, as detailed in Supplementary Table 7.

Then, the NN potential was generated using the method as introduced in our previous work[17]. To pursue a high accuracy for PES, we adopted a large set of power-type structure descriptors, which contained 324 descriptors for every element, including 132 two-body, 170 three-body and 22 four-body descriptors, and compatibly; the network utilized was also large as it involved three-hidden layers (324-80-60-60-1 net), equivalent to 103,743 network parameters in total. Min-max scaling was utilized to normalization the training data sets. Hyperbolic tangent activation functions were used for the hidden layers, whereas a linear transformation was applied to the output layer of all the networks. The limited-memory Broyden–Fletcher–Goldfarb–Shanno method was used to minimize the loss function to match the DFT energy, force and stress. The final energy and force criteria of the r.m.s. errors were around 4.3 meV atom^{-1} and 0.128 eV Å^{-1} respectively. To demonstrate the accuracy of the NN PES, we selected 84 representative ZnCrO crystal structures to compare the NN results with the DFT calculation results. This showed an average energy error of 6.88 meV atom^{-1}, which is quite standard for global NN potentials and accurate enough to search the stable-structure candidates. Details for the comparison between the DFT and NN results are given in Supplementary Table 8.

Finally, SSW–NN simulation was performed over a wide range of composition and structures, both for the global data-set generation and for the final production of the ternary phase diagram in Fig. 1. The data for Fig. 1 were taken from the global minima at each composition of ZnCrO as identified from the SSW–NN simulation, in which each composition is simulated in unit cells of 11–56 and explored to cover more than 10,000 minima on the PES by SSW. Thus, a large variety of structures that ranged from crystalline to amorphous structures were obtained from the SSW–NN simulation. All the low-energy structure

candidates from the SSW–NN exploration were finally verified by plane-wave DFT calculations.

DFT calculations. All the DFT calculations were performed by using the plane-wave VASP code, in which electron–ion interaction is represented by the projector-augmented wave pseudopotential. The exchange functional utilized was the spin-polarized GGA-PBE[28,29] with the local Hubbard term U correction ($U=3.3$ eV) for Cr (ref. [30]) given that ZnCrO structures generally have a strong correlation on Cr atoms. The sensitivity of U was examined by benchmarking with experimental data, which showed that a U value between about 3 and 4 eV can describe well the structure and energy gap for different Cr-based oxides (Supplementary Table 9). The band structure for critical adsorption states was calculated using the hybrid HSE06 functional, which showed a consistent picture with the results from the PBE–U calculation (Supplementary Fig. 9). The kinetic energy cutoff was set as 450 eV. The first Brillouin zone k-point sampling utilizes the Monkhorst–Pack scheme with an automated mesh determined by 25 times the reciprocal lattice vectors for bulk and a $3\times3\times1$ mesh for surface calculations. The energy and force criteria for convergence of the electron density and structure optimization were set at 10^{-6} eV and 0.02 eV Å^{-1}, respectively. For the spinel $ZnCr_2O_4$ phase, the antiferromagnetic state is the ground state, but the ferromagnetic state is only 0.025 eV per $ZnCr_2O_4$ formula unit higher. This small energy difference was found to be typical for other compositions, such as $Zn_3Cr_3O_8$. Owing to the small energy difference, we utilized the ferromagnetic solution to generate the DFT data set for NN training and also to compute the reaction profiles.

The ab initio thermodynamics analyses were performed to determine the equilibrium O_v concentration in ZnCrO bulk and surfaces, in which equation (1) was used to compute the ΔG as a function of temperature and CO/H_2 partial pressure. ΔG was computed with the standard thermodynamics approach by incorporating zero-point energy and entropy contributions to the total energy (Supplementary Information). Based on the stable structures from the SSW–NN and thermodynamics analyses, we determined the CO hydrogenation reaction profile using DFT calculation in combination with the efficient reaction sampling and transition-state search methods developed previously[31,32]. A numerical microkinetics simulation was utilized to solve the rate equations at different reaction conditions.

Data availability

All the data are available within the article (and Supplementary Information) and from the corresponding authors upon reasonable request.

Code availability

The software code for LASP and the NN potentials used within the article are available from the corresponding author upon request or on the website http://www.lasphub.com.

Received: 16 January 2019; Accepted: 3 May 2019;
Published online: 17 June 2019

References

1. Kung, H. H. Methanol synthesis. *Catal. Rev. Sci. Eng.* **22**, 235–259 (1980).
2. Molstad, M. C. & Dodge, B. F. Zinc oxide–chromium oxide catalysts for methanol synthesis. *Ind. Eng. Chem.* **27**, 134–140 (1935).
3. Jiao, F. et al. Selective conversion of syngas to light olefins. *Science* **351**, 1065–1068 (2016).
4. Waugh, K. Methanol synthesis. *Catal. Today* **15**, 51–75 (1992).
5. Dumitru, R. et al. Synthesis, characterization of nanosized $ZnCr_2O_4$ and its photocatalytic performance in the degradation of humic acid from drinking water. *Catalysts* **8**, 210 (2018).
6. Song, H. et al. Spinel-structured $ZnCr_2O_4$ with excess Zn is the active ZnO/Cr_2O_3 catalyst for high-temperature methanol synthesis. *ACS Catal.* **7**, 7610–7622 (2017).
7. Del Piero, G., Trifiro, F. & Vaccari, A. Non-stoichiometric Zn–Cr spinel as active phase in the catalytic synthesis of methanol. *J. Chem. Soc. Chem. Commun.* **00**, 666–658 (1984).
8. Bertoldi, M., Fubini, B., Giamello, E., Trifirò, F. & Vaccari, A. Structure and reactivity of zinc–chromium mixed oxides. Part 1. The role of non-stoichiometry on bulk and surface properties. *J. Chem. Soc. Faraday Trans.* **84**, 1405–1421 (1988).
9. Errani, E., Trifiro, F., Vaccari, A., Richter, M. & Del Piero, G. Structure and reactivity of Zn–Cr mixed oxides. Role of non-stoichiometry in the catalytic synthesis of methanol. *Catal. Lett.* **3**, 65–72 (1989).
10. Bradford, M. C., Konduru, M. V. & Fuentes, D. X. Preparation, characterization and application of Cr_2O_3/ZnO catalysts for methanol synthesis. *Fuel Process. Technol.* **83**, 11–25 (2003).
11. Grimes, R. W., Binks, D. J. & Lidiard, A. The extent of zinc oxide solution in zinc chromate spinel. *Phil. Mag. A* **72**, 651–668 (1995).
12. Shang, C. & Liu, Z.-P. Stochastic surface walking method for structure prediction and pathway searching. *J. Chem. Theory Comput.* **9**, 1838–1845 (2013).
13. Zhang, X.-J., Shang, C. & Liu, Z.-P. From atoms to fullerene: stochastic surface walking solution for automated structure prediction of complex material. *J. Chem. Theory Comput.* **9**, 3252–3260 (2013).
14. Guan, S.-H., Zhang, X.-J. & Liu, Z.-P. Energy landscape of zirconia phase transitions. *J. Am. Chem. Soc.* **137**, 8010–8013 (2015).
15. Zhu, S.-C., Xie, S.-H. & Liu, Z.-P. Nature of rutile nuclei in anatase-to-rutile phase transition. *J. Am. Chem. Soc.* **137**, 11532–11539 (2015).
16. Li, Y.-F., Zhu, S.-C. & Liu, Z.-P. Reaction network of layer-to-tunnel transition of MnO_2. *J. Am. Chem. Soc.* **138**, 5371–5379 (2016).
17. Huang, S.-D., Shang, C., Zhang, X.-J. & Liu, Z.-P. Material discovery by combining stochastic surface walking global optimization with a neural network. *Chem. Sci.* **8**, 6327–6337 (2017).
18. Behler, J. Representing potential energy surfaces by high-dimensional neural network potentials. *J. Phys. Condens. Matter* **26**, 183001–1830024 (2014).
19. Ma, S., Huang, S.-D., Fang, Y.-H. & Liu, Z.-P. TiH hydride formed on amorphous black titania: unprecedented active species for photocatalytic hydrogen evolution. *ACS Catal.* **8**, 9711–9721 (2018).
20. Cheng, K. et al. Direct and highly selective conversion of synthesis gas into lower olefins: design of a bifunctional catalyst combining methanol synthesis and carbon–carbon coupling. *Angew. Chem. Int. Ed.* **128**, 4803–4806 (2016).
21. Riva, A., Trifirò, F., Vaccari, A. & Mintchev, L. Structure and reactivity of zinc–chromium mixed oxides. Part 2. Study of the surface reactivity by temperature-programmed desorption of methanol. *J. Chem. Soc. Faraday Trans.* **84**, 1423–1435 (1988).
22. Giamello, E., Fubini, B., Bertoldi, M. & Vaccari, A. Structure and reactivity of zinc–chromium mixed oxides. Part 3. The surface interaction with carbon monoxide. *J. Chem. Soc. Faraday Trans.* **85**, 237–249 (1989).
23. Tan, L. et al. *Iso*-butanol direct synthesis from syngas over the alkali metals modified Cr/ZnO catalysts. *Appl. Catal. A* **505**, 141–149 (2015).
24. Tian, S. et al. The role of potassium promoter in isobutanol synthesis over Zn–Cr based catalysts. *Catal. Sci. Technol.* **6**, 4105–4115 (2016).
25. Wang, J. et al. A highly selective and stable ZnO–ZrO_2 solid solution catalyst for CO_2 hydrogenation to methanol. *Sci. Adv.* **3**, e1701290 (2017).
26. Behrens, M. et al. The active site of methanol synthesis over Cu/ZnO/Al_2O_3 industrial catalysts. *Science* **336**, 893–897 (2012).
27. Huang, S.-D. et al. LASP: Fast global potential energy surface exploration. *WIREs Compt. Mol. Sci.* https://doi.org/10.1002/wcms.1415 (2019).
28. Blöchl, P. E. Projector augmented-wave method. *Phys. Rev. B* **50**, 17953–17979 (1994).
29. Kresse, G. & Joubert, D. From ultrasoft pseudopotentials to the projector augmented-wave method. *Phys. Rev. B* **59**, 1758–1775 (1999).
30. Yaresko, A. Electronic band structure and exchange coupling constants in ACr_2X_4 spinels (A=Zn, Cd, Hg; X=O, S, Se). *Phys. Rev. B* **77**, 115106 (2008).
31. Zhang, X.-J., Shang, C. & Liu, Z.-P. Double-ended surface walking method for pathway building and transition state location of complex reactions. *J. Chem. Theory Comput.* **9**, 5745–5753 (2013).
32. Zhang, X.-J. & Liu, Z.-P. Variable-cell double-ended surface walking method for fast transition state location of solid phase transitions. *J. Chem. Theory Comput.* **11**, 4885–4894 (2015).

Acknowledgements

This work was supported by the National Key Research and Development Program of China (2018YFA0208600) and the National Science Foundation of China (21573149, 21533001 and 91745201).

Author contributions

Z.-P.L. conceived the project and contributed to the design of the calculations and analyses of the data. S.M. carried out most of the calculations and wrote the draft of the paper. S.-D.H. wrote the neural network code and contributed to the analyses of the data. All the authors discussed the results and commented on the manuscripts.

Competing interests

The authors declare no competing interests.

Additional information

Supplementary information is available for this paper at https://doi.org/10.1038/s41929-019-0293-8.

Reprints and permissions information is available at www.nature.com/reprints.

Correspondence and requests for materials should be addressed to Z.-P.L.

Publisher's note: Springer Nature remains neutral with regard to jurisdictional claims in published maps and institutional affiliations.